NANO LETTERS
Letter
Cite This: *Nano Lett.* 2018, 18, 994−1000
pubs.acs.org/NanoLett

High-Performance Photodetectors Based on Solution-Processed Epitaxial Grown Hybrid Halide Perovskites

Li Ji,[*,†,‡,⊥] Hsien-Yi Hsu,[*,‡,§,∥,⊥] Jack C. Lee,[†] Allen J. Bard,[‡] and Edward T. Yu[*,†]

[†]Microelectronics Research Center, Department of Electrical and Computer Engineering and [‡]Center for Electrochemistry, Department of Chemistry and Biochemistry, the University of Texas at Austin, Austin, Texas 78712, United States
[§]School of Energy and Environment, City University of Hong Kong, Hong Kong, China
[∥]Shenzhen Research Institute of City University of Hong Kong, Shen Zhen, 518057, China

Supporting Information

ABSTRACT: Hybrid organic−inorganic halide perovskites (HOIPs) have recently attracted tremendous attention because of their excellent semiconducting and optoelectronic properties, which exist despite their morphology and crystallinity being far inferior to those of more mature semiconductors, such as silicon and III−V compound semiconductors. Heteroepitaxy can provide a route to achieving high-performance HOIP devices when high crystalline quality and smooth morphology are required, but work on heteroepitaxial HOIPs has not previously been reported. Here, we demonstrate epitaxial growth of methylammonium lead iodide ($MAPbI_3$) on single crystal KCl substrates with smooth morphology and the highest carrier recombination lifetime (~213 ns) yet reported for nonsingle crystalline $MAPbI_3$. Experimental Raman spectra agree well with theoretical calculations, presenting in particular a sharp peak at 290 cm^{-1} for the torsional mode of the organic cations, a marker of orientational order and typically lacking in previous reports. Photodetectors were fabricated showing excellent performance, confirming the high quality of the epitaxial $MAPbI_3$ thin films. This work provides a new strategy to enhance the performance of all HOIPs-based devices.

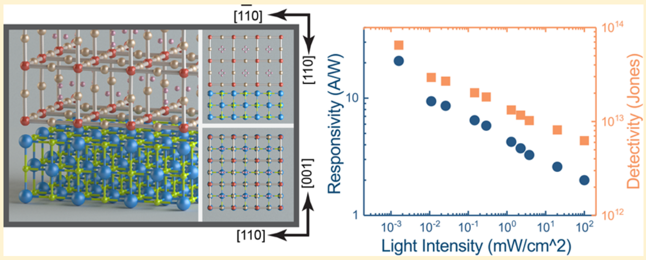

KEYWORDS: *Perovskites, epitaxial, photodetectors, solution-processed*

Hybrid organic−inorganic halide perovskites (HOIPs) have been intensively studied in recent years, because they are solution processable, require only earth-abundant elements and yield excellent semiconducting and optoelectronic properties.[1−17] Of particular interest have been applications in photovoltaics and optoelectronic devices with the certified efficiency of hybrid halide perovskite-based solar cells having increased from 3.8%[18] to 22.1%[19] in only 6 years. The theoretical limit of HOIP-based photovoltaic energy conversion efficiency has been estimated to be 31%,[20] which is very close to the Shockey-Queisser limit of GaAs solar cells (33%). In addition, HOIPs have shown great potential for photodetector applications.[21−23]

For thin film optoelectronic devices, morphology and crystal quality are critical for obtaining high performance, as confirmed in previous studies of HOIP-based devices.[15,24−28] Numerous approaches have been used to modify their film morphology and improve crystallinity, including but not limited to various postannealing methods, for example, vacuum-assist/pressure-assist/oxygen-assist/two-step annealing, optimizing precursor and Lewis acid−base adduct approach.[26,29−32] However, the morphology and crystallinity of thin film HOIPs remain far inferior to those of more mature photovoltaic materials, such as silicon and III−V compound semiconductors.

Heteroepitaxy-growth of a crystalline film atop a different substrate material surface with atomically aligned orientation is the basis for crystalline semiconductor multijunction solar cells, quantum cascade lasers, light-emitting diodes, and other optoelectronic devices in which high crystalline quality and smooth surface morphology are required. The prevailing approaches for heteroepitaxial growth generally rely on various vacuum deposition methods, such as molecular-beam epitaxy, atomic-layer epitaxy, and metal−organic vapor-phase epitaxy. However, the high cost of vacuum-based deposition techniques has driven interest in finding low cost alternatives, and growth of various heteroepitaxial films has also been demonstrated using low-cost solution-based processes.[33,34] The compatibility of HOIPs with low cost solution-based processes suggests that this approach might enable heteroepitaxial growth of high quality HOIP thin films with substantially improved optoelectronic properties. However, no work has been reported to date on heteroepitaxial growth of HOIP thin films.

Though not sufficient, compatible crystal symmetry and lattice match are powerful factors influencing heteroepitaxial

Received: October 18, 2017
Revised: December 22, 2017
Published: January 5, 2018

DOI: 10.1021/acs.nanolett.7b04445
Nano Lett. 2018, 18, 994−1000

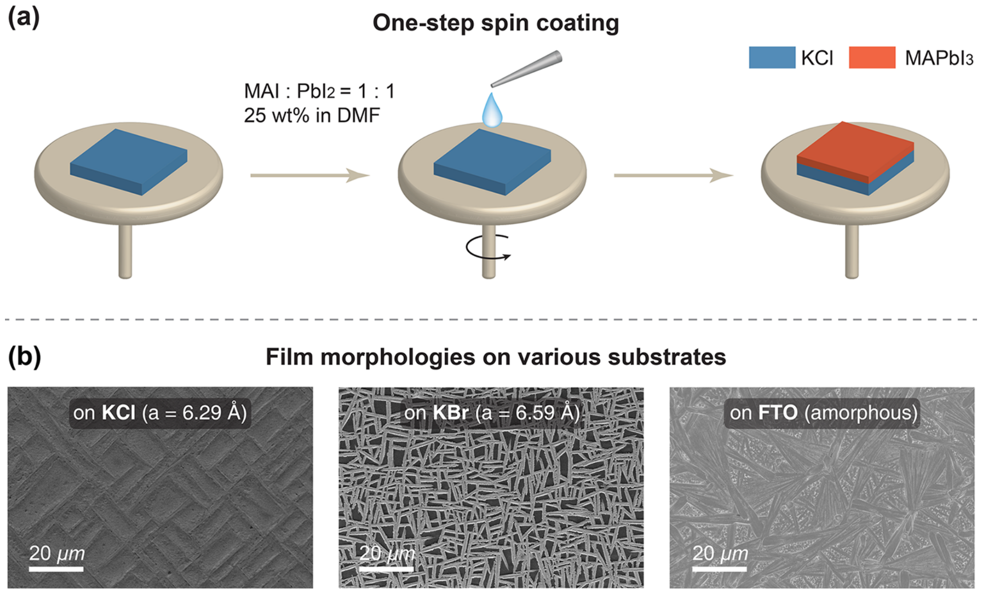

Figure 1. Processing scheme for perovskite thin film via one-step spin coating and film morphology on various substrates (a) One-step spin-coating scheme for thin film deposition, using a 1:1 ratio (molar) of MAI and PbI_2 in DMF. (b) SEM characterization of $MAPbI_3$ thin films on KCl (001), KBr (001) and FTO coated-glass.

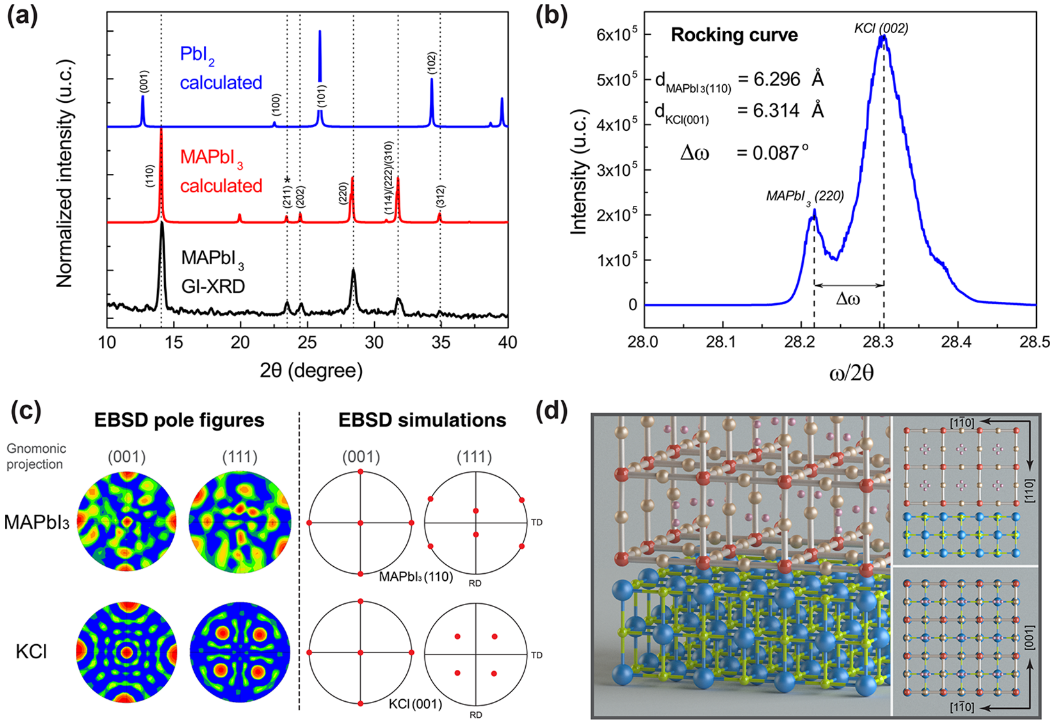

Figure 2. X-ray diffraction (XRD) and electron backscatter diffraction (EBSD) chracterization for determing crystal quality and expitaxial orientation. (a) Grazing incidence X-ray diffraction (GI-XRD) measured for $MAPbI_3$ on KCl (black line) and calculated spectra for tegragonal $MAPbI_3$ and PbI_2. (b) Rocking-curve spectra for $MAPbI_3$ on KCl at angle $2\theta = 28.3°$. (c) Experimental measurements and simulations of pole figures from EBSD mapping for both $MAPbI_3$ and KCl. The simulations are obtained by gnomonic projection of $MAPbI_3$ (110) and/or KCl (001) on (001) and (111) planes. (d) Three-dimensional rendering of atomic arrangement for expitaxial $MAPbI_3$ on KCl. Colors represent the following: blue, K atom; green, Cl atom; heavy brown, I atom; light brown, Pb atom; pink, CH_3 and/or NH_3 cation groups. The inset is top view.

growth. Methylammonium lead iodide ($MAPbI_3$), one of the most widely studied HOIPs, has a quasi-cubic (tetragonal, space group *I*4/*mcm*, *Z* = 4) structure at room temperature with its quasi-cubic lattice constant being approximately 6.31 Å. Potassium chloride (KCl), a common rocksalt, has a face-centered cubic structure with lattice constant *a* = 6.29 Å. The lattice mismatch of $MAPbI_3$(110)/KCl(001) is calculated to be only 0.3% at room temperature, favorable for heteroepitaxy. Here in this work, we demonstrate the heteroepitaxial growth of $MAPbI_3$ on KCl (100) with the resulting epitaxial films exhibiting excellent morphology, crystallinity, and carrier lifetime. A high-performance photodetector is fabricated to validate the high quality of these thin films.

DOI: 10.1021/acs.nanolett.7b04445
Nano Lett. 2018, 18, 994−1000

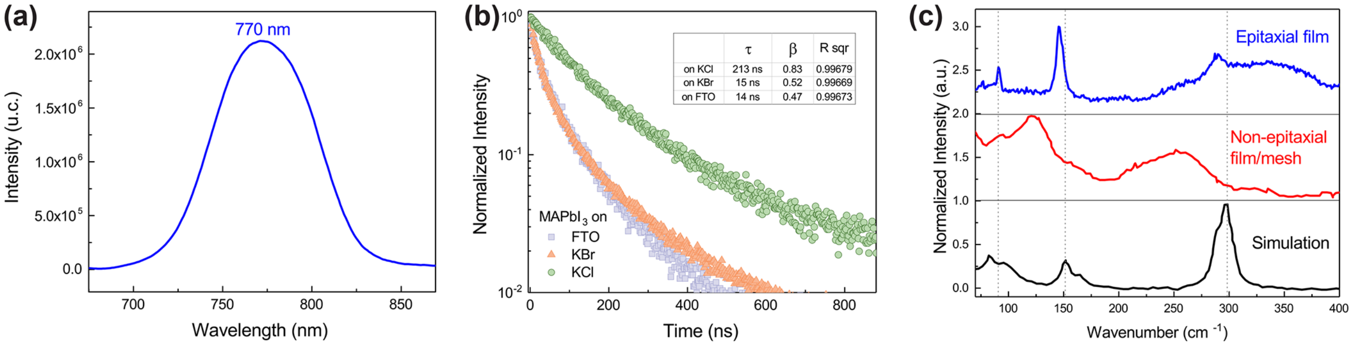

Figure 3. Optical properties of the perovskite films. (a) Steady-state photoluminescence (PL) spectra of MAPbI3 films on KCl at room temperature. The PL excitation wavelength was 530 nm. (b) Normalized time-resolved PL spectra taken at the peak emission wavelength of 770 nm for $MAPbI_3$ films on KCl (green circles), on KBr (orange triangle), and on FTO glass (blue squares), respectively. Solid lines are single stretched exponential fits, with parameters listed in the inset table. Carrier life times, τ, were extracted directly from the fitted curves. A pulsed laser diode (pulse duration <200 ps, fluence ~30 nJ/cm^2) at 530 nm was used as excitation source. All films were coated with PMMA to prevent degradation. (c) The measured Raman spectra of $MAPbI_3$ on KCl (red line), on KBr and calculated spectra (black line). The laser excitation wavelength is 532 nm.

Thin Films Deposition and Characterizations. As illustrated in Figure 1a, a one-step spin-coating process is employed in which the inorganic and organic precursors are mixed in a single solution, a film is deposited by spin coating, and then annealing is used to form the appropriate crystalline phase. In general, it is challenging to form a smooth and continuous perovskite film by one-step solution coating. A noncontinuous perovskite film containing pin holes is usually obtained, and the incomplete coverage of the perovskite films typically results in poor device performance. In contrast, the approach employed here results in continuous thin films on KCl (001) substrates, as shown in Figure 1b. Furthermore, we observe highly oriented, aligned, mesh-like microstructure across the whole sample surface, suggesting that heteroepitaxial growth occurs over the entire substrate. The thickness of epitaxial films is 200−300 nm. However, for thin films on KBr for which the lattice constant is slightly larger (6.59 Å) and whose lattice mismatch with $MAPbI_3$ is 4.4% the meshlike microstructures seen in Figure 1b are not consistently oriented, which we attribute to nonepitaxial growth. The same occurs for thin films on amorphous FTO-coated glass, also shown in Figure 1b. For films deposited on both KBr and FTO, pin-holes and voids are present in the deposited film, as commonly seen in previous reports.[35,36]

To determine the crystal quality and expitaxial orientation of $MAPbI_3$ films deposited on KCl (001), X-ray diffraction (XRD) and electron backscatter diffraction (EBSD) characterization were performed. XRD patterns were obtained to characterize the crystallinity of $MAPbI_3$ films on KCl, as shown in Figure 2a,b. The standard symmetrical scan mode for thin films is not suitable, as the peaks from the perovskite thin films are overwhelmed by the presence of strong peaks from the KCl substrate. We therefore employed grazing incidence X-ray diffraction (GI-XRD) to limit the substrate signal. In Figure 2a, XRD patterns calculated for PbI_2 (blue line) and tetragonal $MAPbI_3$ (red line) are shown, along with the GI-XRD experimental spectra for $MAPbI_3$ on KCl (black line). No PbI_2 peaks are observed in the experimental measurement, indicating complete formation of $MAPbI_3$ after spin-coating and annealing. The peaks calculated for the tetragonal phase of $MAPbI_3$ and those in the measured GI-XRD experimental pattern are in excellent agreement, confirming the good crystallinity and the dominant (110) phase. The peak associated with reflection from the (211) plane, which is the characteristic peak for distinguishing between the cubic and tetragonal phases, is labeled by an asterisk.

Rocking-curve (RC) measurements, performed by fixing the detector at the center of the expected Bragg reflection and tilting the sample, are a powerful way to characterize favored growth directions and heteroepitaxial quality. Defects such as mosaicity, dislocations, or curvature lead to broadening of RC peaks. For example, the broad RC peaks observed in previous studies ($MAPbI_3$ on TiO_2) were attributed to the poor favored orientation.[37] Figure 2b shows the RC measured for $MAPbI_3$/KCl at a Bragg angle of 2θ = 28.3°, corresponding to the $MAPbI_3$ (220) and KCl (002) diffraction peak visible in the θ-2θ scan in Figure 2a. There is a clear $MAPbI_3$ (220) peak in the RC plot with full width at half-maximum (fwhm) of 0.039°, indicating high quality heteroepitaxial growth.[37]

The RC spectrum in Figure 2b provides lattice constants in the out-of-plane direction, but for characterizing heteroepitaxial growth details for the in-plane direction are also required. Cross-sectional transmission electron microscopy (CS-TEM) is typically used to visualize the lattice match and heteroepitaxy directly. However, the low thermal tolerance and instability to humidity of hybrid trihalide perovskites make CS-TEM highly challenging. Here, EBSD is used as an alternative and serves to reveal the orientation of the epitaxial layer with respect to the crystalline substrate.[38] To study the relative orientation, samples for EBSD were selected with a portion of the KCl substrate left uncovered by $MAPbI_3$. First, a backscatter Kikuchi diffraction pattern (BKD) of the exposed KCl substrate is taken to establish a reference in the microscope system. Then, mapping of the BKD patterns of both the exposed KCl substrate area and $MAPbI_3$ film area was performed simultaneously to determine their relative orientation. Because every Kikuchi pattern contains complete information about the film or crystal orientation, texture pole figures can be obtained, as shown in Figure 2c. The expected KCl (001) orientation is confirmed by comparing the measured texture pole figures with EBSD simulations. For the $MAPbI_3$ film, the texture pole figures agree well with simulations for $MAPbI_3$ in the (110) orientation, proving the epitaxial relationship of $MAPbI_3$ (110) relative to the KCL substrate. As illustrated in Figure 2d, the inorganic PbI_6 octahedral cage in the $MAPbI_3$ is well matched to the KCl lattice matrix. On the basis of the expectation that Pb/Cl and K/I should form strong ionic bonds, we suggest, as shown in Figure 2b, that Pb atoms are positioned atop Cl

DOI: 10.1021/acs.nanolett.7b04445
Nano Lett. 2018, 18, 994−1000

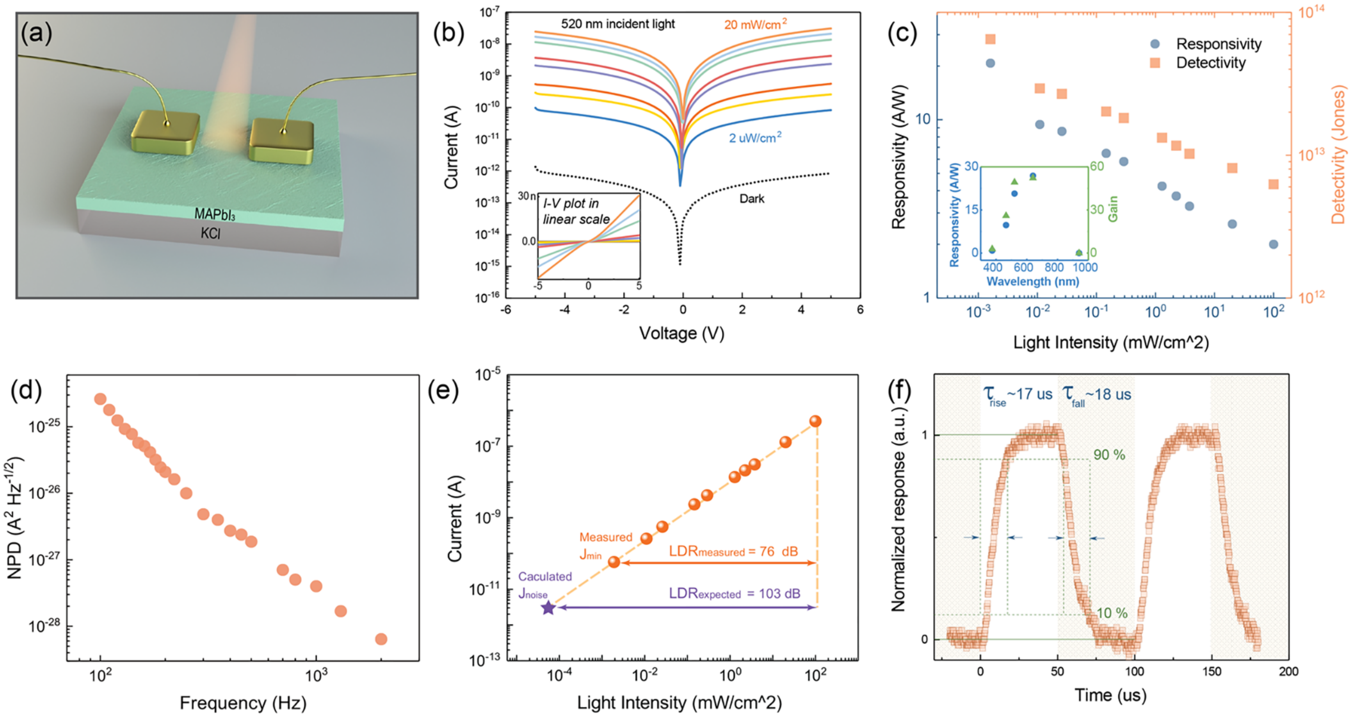

Figure 4. Characterization of photodetectors (a) Schematic illustration of $MAPbI_3$ photodetectors. (b) *I*−*V* curves of the photodetector measured under dark and various light illumination (520 nm), respectively. The inset is *I*−*V* curves plotted under linear scale. (c) Plots of resonsivity and detectivity as a function of incident light intensity (520 nm wavelength). The inset is responsivity and gain versus incident light wavelength. (d) Noise power density spectrum of the photodetector measured from 100 to 2000 Hz under dark with 0 V bias. (e) Irradiance-dependent photocurrent at a bias of 5 V as a function of light intensity. (f) Frequency response of photodetectors. The size of the photodetector is 500 μm^2.

atoms and I atoms atop K atoms. MA^+ cation groups in the intermediate interface sit on Cl sites, which is expected to stabilize the interfacial structures.

Direct optical characterization of the epitaxial films provides additional evidence confirming the high film quality. Figure 3a shows the steady-state room temperature photoluminescence (PL) spectrum of a representative $MAPbI_3$ film on KCl, exhibiting a strong peak at 770 nm. In order to prevent degradation during measurement, all samples for optical measurements were sealed by spin-coating a layer of poly methyl methacrylate (PMMA) atop thin films. Time-resolved PL measurements, obtained at the peak emission wavelength of 770 nm with a pulsed LED laser excitation at 530 nm, are shown in Figure 3b. Both time-resolved PL decay spectra were fitted using a single stretched exponential function

$$I(t) = I_0 + I_1 e^{-(t/\tau)^{\beta}} \qquad (1)$$

where t is time, τ is the carrier lifetime, and β is the stretch index. As shown in the inset table of Figure 3b, the unquenched carrier lifetime for $MAPbI_3$ on KCl is 213 ns, the highest reported value for nonsingle crystalline $MAPbI_3$ thin films.[14,15,17,39−41] The carrier diffusion length L_D can be estimated as $L_D = \sqrt{D\tau}$, where D is the diffusion coefficient. Using the previously reported values for D[42] of 0.036 cm^2/s for electrons and 0.022 cm^2/s for holes, the calculated diffusion lengths for electrons and holes in epitaxial $MAPbI_3$ thin films on KCl are 875 and 684 nm, respectively, much larger than the film thickness (200−300 nm). For $MAPbI_3$ on FTO glass, the carrier lifetime is 14 ns, most likely due to the poor crystalline quality and surface coverage of the thin films on FTO. The stretch index is only 0.47, suggesting a large degree of disorder in the material and/or large amount of nonradiative recombination at localized trap states or surface states.

Raman spectroscopy can also serve as a powerful probe of crystal quality, bonding configuration, and local molecular vibrational modes. However, only a limited number of Raman spectroscopic studies have been reported for $MAPbI_3$; these generally lack sharp peaks and often suffer from significant discrepancies between experimental results and simulations,[43−47] due to the high sensitivity of Raman spectra to film quality and morphology.[47] Brivio et al.[45] and Quarti et al.[47] both performed theoretical simulations of $MAPbI_3$ Raman spectra using DFT calculations, assigning a peak at 95 cm^{-1} to the stretching of Pb−I bonds, a 151 cm^{-1} peak to a libration mode of the MA^+ cations and a 300 cm^{-1} peak to a torsional mode of the MA^+ cations. As shown in Figure 3c, the Raman spectra of the $MAPbI_3$/KCl thin films in this work contain a clear peak at 91 cm^{-1}, corresponding to the vibrational modes of the inorganic PbI_6 octahedra cage. The peak at 146 cm^{-1} is attributed to librations of the organic cations, slightly red-shifted compared to the numerically simulated value. The torsional mode, corresponding to rotation of CH_3 units against the NH_3 units along the C−N axis in the tetragonal phase, is predicted to be around 300 cm^{-1} by Brivio et al. and Quarti et al.; however, this peak was not observed in their experiments. In this work, the restricted torsional mode of the MA^+ cations is clearly observed at 290 cm^{-1}, in agreement with their theoretical calculations. It has been suggested that the organic cation rotation in tetragonal $MAPbI_3$ can lower the exciton binding energy and slow carrier recombination, critical for solar photovoltaic applications.[48,49] Thus, the Raman results indicates the reduced capture of carriers by nonradiative trap

Table 1. Device Performance Comparison between Epitaxial $CH_3NH_3PbI_3$ Thin Film Photodetectors in This Work and Other Reported $CH_3NH_3PbI_3$-Based Photodetectors from Literature

device type	materials/structure	responsivity R (A W^{-1})	detectivity D^* (Jones)	rise time τ_r (μs)	voltage (V)	reference
photoconductors (lateral structure)	Single-crystal $CH_3NH_3PbI_3$ NW	13.57	5.2×10^{12}	200	5	51
	$CH_3NH_3PbI_3$ epitaxial thin film	20.7	6.5×10^{13}	<17	5	this work
	$CH_3NH_3PbI_3$ thin film	3.49		100	3	52
	$CH_3NH_3PbI_3$ thin film	0.055		50	10	53
	$CH_3NH_3PbI_3$ NW	1.30		200	30	54
	$CH_3NH_3PbI_3$ NW	0.005		300	1	55
	$CH_3NH_3PbI_3$ NW network	0.10	1.02×10^{12}	300	10	56
	single-crystal $CH_3NH_3PbI_3$ NW	4.95	2×10^{13}	100	2	57
photodiodes (vertical structure)	TiO_2/ $CH_3NH_3PbI_3$/SpiroOMeTAD	0.35	1×10^{11}		1	58
	ITO/$CH_3NH_3PbI_3$/TPD-Si_2	242		40	1	21
phototransistors (three terminals)	$CH_3NH_3PbI_3$/PbSe QD	1.2	1×10^8	3000	1	59
	$CH_3NH_3PbI_3$/Graphene	1.9×10^4	2.7×10^8	10000	2	60
	$CH_3NH_3PbI_3$/MoS_2	1.9×10^6	1.3×10^{12}	600000	5	61
	silicon diode	0.6	1×10^{12}	10 ns	5	

states. This result also helps to explain the long carrier lifetimes obtained in this work.

Performance of Photodetectors. For HOIP device studies, it is typical to fabricate a photovoltaic device for characterizing optoelectronic performance, usually employing a vertical device architecture. In this work, however, KCl is a nonconducting substrate so that a horizontal architecture must be used. Using shadow mask patterning, we fabricated photodetectors with two metal contacts deposited atop $MAPbI_3$ thin films, as illustrated in Figure 4a. To characterize the photodetector, we used a light-emitting diode operating at 520 nm as a monochromatic light source. Typical $I-V$ characteristics of the detectors at different illumination intensities are shown in Figure 4b. The dark current is extremely low, ~0.2 pA at 1 V bias, and the photocurrent to dark current ratio is very high: $I_{light}/I_{dark} > 1 \times 10^4$ at 20 mW/cm^2 and $I_{light}/I_{dark} > 1 \times 10^2$ at 2 uW/cm^2.

The performance of photodetectors is conventionally assessed using several figures of merit. Responsivity (R), which relates the generated photocurrent to a given incident power, indicates how efficiently the detector responds to an optical signal. The spectral responsivity is expressed as $R = J_{light}/P$, where J_{light} is the photocurrent density and P is incident light intensity. As shown in Figure 4c, R is as high as 20.7 A/W at 5 V bias with 2 uW/cm^2 illumination under 520 nm. Photoconductive gain, given by $G = R \times E_{hv}$, which quantifies the ability to provide multiple electrical carriers per single incident photon where E_{hv} is the energy of the incident photon, is shown in the inset to Figure 4c. The responsivity and gain, which are very high in comparison to values in the literature for HOIPs or conventional semiconductors as shown in Table 1, are attributed to the high carrier mobility and long carrier lifetime of epitaxial film. Detectivity ($D = J_{light}/(P \times (2qJ_{dark})^{1/2})$, another important figure of merit for photodetectors, reflects the ability to detect weak optical signals.[50] As shown in Figure 4c, the maximum detectivity is 6.5×10^{13} Jones, the highest value yet reported for $MAPbI_3$-based photoconductors, owing to a small J_{dark}, due to low recombination rates and low thermal emission rates.

Linear dynamic range (LDR), which measures the range of incident light irradiances over which the photoresponse is linear, is critical for image sensing applications. It is expressed as LDR = $20 \times \log(J_{upper}/J_{lower})$, where J_{upper} and J_{lower} are the limits of the current values for which linear response is observed. As shown in Figure 4e, the extracted LDR in this work is 76 dB, higher than that of commercial InGaAs photodetectors (66 dB). It is worth noting that for the upper limit, the current within the linear region and the highest light intensity are limited by the light source we use. In addition, the minimum detectable light intensity is governed by the light power meter we use. To gain a more accurate view of actual LDR, the dark noise current was measured to further estimate the LDR value,[51] as shown in Figure 4d. The expected LDR is 103 dB, comparable to that of a Si photodiode (120 dB). Another important parameter for photodetectors is response speed. As shown in Figure 4f, the rise time (τ_{rise}) and fall time (τ_{fall}) are approximately 17 us. It is worth noting that the speed measured here is limited by the long rise time of the LED used, ~ 14 us. The actual speed of the photodetector is expected to be even faster, owing to the high quality of epitaxial thin film.

Table 1 shows a comparison of the performance of several $MAPbI_3$-based photodetectors. On the basis of the device architecture, the photodetectors can be categorized into photoconductor-type, photodiode-type, and phototransistor-type. Compared with previously reported $MAPbI_3$-based photoconductor-type detectors, the photodetectors in this work on epitaxial films exhibit much higher responsivity and detectivity and much faster response time, confirming the high quality of the $MAPbI_3$ film, and consistent with the long carrier life times discussed above.

In summary, in this work we demonstrate the heteroepitaxial growth of hybrid organic–inorganic halide perovskites, which we achieve using closely lattice matched rock salt substrates. The epitaxial relationship with the substrate and high crystalline quality of $MAPbI_3$ films on KCl substrates are confirmed using X-ray diffraction, EBSD, and Raman spectroscopy. Time-resolved PL reveals carrier lifetimes that are the longest yet reported for nonsingle crystalline $MAPbI_3$ thin films, leading to outstanding performance of lateral photodetectors fabricated from these films. This work demonstrates a new strategy for engineering hybrid halide perovskites based devices, including photovoltaic, photodetectors, and light-emitting devices.

Methods. *Material Synthesis and Characterization.* Methylamine iodide (MAI) was prepared by reacting methylamine, 33 wt % in ethanol (Sigama-Aldrich) with hydroiodic acid (HI) 57 wt % in water (Sigma-Aldrich) at room temperature. After drying at 100 °C, white powder was formed, followed by overnight drying in a vacuum oven. To form the precursor solution, MAI and PbI_2 (Sigama-Aldrich) were dissolved in anhydrous *N*,*N*-dimethylformamide (DMF) at a 1:1 molar ratio. The prepared precursor was spin-coated on KCl(001) substrate at 2000 rpm in a Ar-filled golvebox. After the spin-coating, the films were annealed at 100 °C for 20 min. For photodetector fabrication, Au metal contacts were deposited directly onto perovskite thin film by e-beam evaporation through a stainless steel shadow mask. The temperature was monitored and kept under 40 °C during deposition.

A field emission scanning electron microscopy (SEM) system (Zeiss) was used to acquire SEM figures. The beam voltage is 2 kV to minimize electron-induced damage. Steady-state and time-resolved PL measurements were acquired using a time-correlated single photon counting setup. Film samples were photoexcited using a laser head pulsed, providing <200 ps pulses with the fluence of ~30 nJ/cm^2. The Raman measurements were performed with excitation lines of 532 nm. Laser power density was 1 mW. XRD were obtained using a double-axis high resolution X-ray diffractometer, using CuKα ($\lambda = 1.5405$ Å) radiation source. The X-ray generator was set to 40 kV and 45 mA. The EBSD patterns were obtained in a SEM system (Zeiss Neon 40 FE-SEM) equipped with an EDAX (Mahwah, NJ) APEX 2 integrated EDS and EBSD system by focusing the electron beam onto the sample surface at a tilt angle of 70° with respect to the horizontal. The scanned data were post analyzed using the EDAX TSL OIM 5.0 software.

Photodetector Characterization. Photodetectors were characterized using a B1500A Semiconductor Device Analyzer (Agilent Technologies) and Summit 11000 AP probe station (Cascade Microtech). The monochromatic light at different wavelengths was provided by light-emitting diode (LED) illumination and the intensity was calibrated by an optical power meter (1830-C, Newport). For transient response measurement, the LED was powered by a pulse pattern generator (Agilent 81110A). Photocurrent from the photodetectors was amplified via a low noise current preamplifier (SR570, Stanford) and the output signal was monitored by measuring voltage across a 100 ohm resistor by a digital oscilloscope (3034T, Agilent) with 50 ohm input impedance. Dark current noise was measured using a SR830 lock-in-amplifier (Stanford) with testing performed in an electrically shielded and optically sealed probe station on a floating table to minimize vibrational noise.

■ ASSOCIATED CONTENT

Ⓢ Supporting Information

The Supporting Information is available free of charge on the ACS Publications website at DOI: 10.1021/acs.nanolett.7b04445.

Details of device fabrication and characterization (PDF)

■ AUTHOR INFORMATION

Corresponding Authors

*E-mail: nmgjili@utexas.edu.
*E-mail: sam.hyhsu@cityu.edu.hk.
*E-mail: ety@ece.utexas.edu.

ORCID

Li Ji: 0000-0002-2004-230X
Allen J. Bard: 0000-0002-8517-0230

Author Contributions

[⊥]L.J. and H.-Y.H. contributes equally.

Notes

The authors declare no competing financial interest.

■ ACKNOWLEDGMENTS

This work was performed in part at the University of Texas Microelectronics Research Center, a member of the National Nanotechnology Coordinated Infrastructure (NNCI), which is supported by the National Science Foundation (Grant ECCS-1542159). This work was partially supported by the Global Climate and Energy Project (GCEP, Agreement No. 60853646-118146). The authors acknowledge the Judson S. Swearingen Regents Chair in Engineering at the University of Texas at Austin. The authors also acknowledge financial support from the Strategic Research Grant (Grants 7004928, 6000595, 7200525, and 9680208) and SZSTI Grant (Grant R-IND12301) at City University of Hong Kong.

■ REFERENCES

(1) Lee, M. M.; Teuscher, J.; Miyasaka, T.; Murakami, T. N.; Snaith, H. J. *Science* **2012**, *338* (6107), 643−647.

(2) Liu, M.; Johnston, M. B.; Snaith, H. J. *Nature* **2013**, *501* (7467), 395−398.

(3) Im, J.-H.; Jang, I.-H.; Pellet, N.; Grätzel, M.; Park, N.-G. *Nat. Nanotechnol.* **2014**, *9* (11), 927−932.

(4) Jeon, N. J.; Noh, J. H.; Kim, Y. C.; Yang, W. S.; Ryu, S.; Seol, S. *Nat. Mater.* **2014**, *13* (9), 897−903.

(5) Mei, A.; Li, X.; Liu, L.; Ku, Z.; Liu, T.; Rong, Y.; Xu, M.; Hu, M.; Chen, J.; Yang, Y.; Grätzel, M.; Han, H. *Science* **2014**, *345* (6194), 295−298.

(6) Zhou, H.; Chen, Q.; Li, G.; Luo, S.; Song, T.-b.; Duan, H.-S.; Hong, Z.; You, J.; Liu, Y.; Yang, Y. *Science* **2014**, *345* (6196), 542−546.

(7) Chen, W.; Wu, Y.; Yue, Y.; Liu, J.; Zhang, W.; Yang, X.; Chen, H.; Bi, E.; Ashraful, I.; Graetzel, M.; Han, L. *Science* **2015**, *350* (6263), 944−948.

(8) Dong, Q.; Fang, Y.; Shao, Y.; Mulligan, P.; Qiu, J.; Cao, L.; Huang, J. *Science* **2015**, *347* (6225), 967−970.

(9) Dou, L.; Wong, A. B.; Yu, Y.; Lai, M.; Kornienko, N.; Eaton, S. W.; Fu, A.; Bischak, C. G.; Ma, J.; Ding, T.; Ginsberg, N. S.; Wang, L.-W.; Alivisatos, A. P.; Yang, P. *Science* **2015**, *349* (6255), 1518−1521.

(10) Jeon, N. J.; Noh, J. H.; Yang, W. S.; Kim, Y. C.; Ryu, S.; Seo, J.; Seok, S. I. *Nature* **2015**, *517* (7535), 476−480.

(11) Nie, W.; Tsai, H.; Asadpour, R.; Blancon, J.-C.; Neukirch, A. J.; Gupta, G.; Crochet, J. J.; Chhowalla, M.; Tretiak, S.; Alam, M. A.; et al. *Science* **2015**, *347* (6221), 522−525.

(12) Ning, Z.; Gong, X.; Comin, R.; Walters, G.; Fan, F.; Voznyy, O.; Yassitepe, E.; Buin, A.; Hoogland, S.; Sargent, E. H. *Nature* **2015**, *523* (7560), 324−328.

(13) Saidaminov, M. I.; Abdelhady, A. L.; Murali, B.; Alarousu, E.; Burlakov, V. M.; Peng, W.; Dursun, I.; Wang, L.; He, Y.; Maculan, G.; Goriely, A.; Wu, T.; Mohammed, O. F.; Bakr, O. M. *Nat. Commun.* **2015**, *6*, 7586.

(14) Shi, D.; Adinolfi, V.; Comin, R.; Yuan, M.; Alarousu, E.; Buin, A.; Chen, Y.; Hoogland, S.; Rothenberger, A.; Katsiev, K.; Losovyj, Y.; Zhang, X.; Dowben, P. A.; Mohammed, O. F.; Sargent, E. H.; Bakr, O. M. *Science* **2015**, *347* (6221), 519−522.

(15) de Quilettes, D. W.; Vorpahl, S. M.; Stranks, S. D.; Nagaoka, H.; Eperon, G. E.; Ziffer, M. E.; Snaith, H. J.; Ginger, D. S. *Science* **2015**, *348* (6235), 683−686.

(16) Yang, Y.; Ostrowski, D. P.; France, R. M.; Zhu, K.; van de Lagemaat, J.; Luther, J. M.; Beard, M. C. *Nat. Photonics* **2016**, *10* (1), 53−59.

(17) Stranks, S. D.; Eperon, G. E.; Grancini, G.; Menelaou, C.; Alcocer, M. J.; Leijtens, T.; Herz, L. M.; Petrozza, A.; Snaith, H. J. *Science* **2013**, *342* (6156), 341−344.

(18) Kojima, A.; Teshima, K.; Shirai, Y.; Miyasaka, T. *J. Am. Chem. Soc.* **2009**, *131* (17), 6050−6051.

(19) *Research Cell Efficiency Records*; National Renewable Energy Laboratory (NREL), 2016; Dec 13, 2017.

(20) Sha, W. E. I.; Ren, X.; Chen, L.; Choy, W. C. *Appl. Phys. Lett.* **2015**, *106* (22), 221104.

(21) Dong, R.; Fang, Y.; Chae, J.; Dai, J.; Xiao, Z.; Dong, Q.; Yuan, Y.; Centrone, A.; Zeng, X. C.; Huang, J. *Adv. Mater.* **2015**, *27* (11), 1912−8.

(22) Li, F.; Ma, C.; Wang, H.; Hu, W.; Yu, W.; Sheikh, A. D.; Wu, T. *Nat. Commun.* **2015**, *6*, 8238.

(23) Fang, Y.; Dong, Q.; Shao, Y.; Yuan, Y.; Huang, J. *Nat. Photonics* **2015**, *9* (10), 679−686.

(24) Yang, W. S.; Noh, J. H.; Jeon, N. J.; Kim, Y. C.; Ryu, S.; Seo, J.; Seok, S. I. *Science* **2015**, *348* (6240), 1234−1237.

(25) Xiao, Z.; Wang, D.; Dong, Q.; Wang, Q.; Wei, W.; Dai, J.; Zeng, X.; Huang, J. *Energy Environ. Sci.* **2016**, *9* (3), 867−872.

(26) Li, X.; Dar, M. I.; Yi, C.; Luo, J.; Tschumi, M.; Zakeeruddin, S. M.; Nazeeruddin, M. K.; Han, H.; Graetzel, M. *Nat. Chem.* **2015**, *7* (9), 703−711.

(27) Zhang, W.; Saliba, M.; Moore, D. T.; Pathak, S. K.; Hörantner, M. T.; Stergiopoulos, T.; Stranks, S. D.; Eperon, G. E.; Alexander-Webber, J. A.; Abate, A.; et al. *Nat. Commun.* **2015**, *6*, 6142.

(28) Eperon, G. E.; Burlakov, V. M.; Docampo, P.; Goriely, A.; Snaith, H. J. *Adv. Funct. Mater.* **2014**, *24* (1), 151−157.

(29) Xie, F. X.; Zhang, D.; Su, H.; Ren, X.; Wong, K. S.; Grätzel, M.; Choy, W. C. H. *ACS Nano* **2015**, *9* (1), 639−646.

(30) Liang, Q.; Liu, J.; Cheng, Z.; Li, Y.; Chen, L.; Zhang, R.; Zhang, J.; Han, Y. *J. Mater. Chem. A* **2016**, *4* (1), 223−232.

(31) Xiao, J.; Yang, Y.; Xu, X.; Shi, J.; Zhu, L.; Lv, S.; Wu, H.; Luo, Y.; Li, D.; Meng, Q. *J. Mater. Chem. A* **2015**, *3* (10), 5289−5293.

(32) Hsu, H. L.; Chen, C. P.; Chang, J. Y.; Yu, Y. Y.; Shen, Y. K. *Nanoscale* **2014**, *6* (17), 10281−10288.

(33) Lange, F. F. *Science* **1996**, *273* (5277), 903−909.

(34) Haber, T.; Andreev, A.; Thierry, A.; Sitter, H.; Oehzelt, M.; Resel, R. *J. Cryst. Growth* **2005**, *284* (1−2), 209−220.

(35) Wang, Q.; Shao, Y.; Dong, Q.; Xiao, Z.; Yuan, Y.; Huang, J. *Energy Environ. Sci.* **2014**, *7* (7), 2359−2365.

(36) Zhou, X.; Bao, C.; Li, F.; Gao, H.; Yu, T.; Yang, J.; Zhu, W.; Zou, Z. *RSC Adv.* **2015**, *5* (72), 58543−58548.

(37) Pellegrino, G.; Colella, S.; Deretzis, I.; Condorelli, G. G.; Smecca, E.; Gigli, G.; La Magna, A.; Alberti, A. *J. Phys. Chem. C* **2015**, *119* (34), 19808−19816.

(38) Shao, Y.; Dai, Y.; Hao, X.; Wu, Y.; Zhang, L.; Zhang, H.; Tian, Y. *CrystEngComm* **2013**, *15* (39), 7965.

(39) Yuan, S.; Qiu, Z.; Zhang, H.; Gong, H.; Hao, Y.; Cao, B. *Appl. Phys. Lett.* **2016**, *108* (3), 033904.

(40) You, J.; Meng, L.; Song, T.-B.; Guo, T.-F.; Yang, Y.; Chang, W.-H.; Hong, Z.; Chen, H.; Zhou, H.; Chen, Q.; Liu, Y.; De Marco, N.; Yang, Y. *Nat. Nanotechnol.* **2015**, *11* (1), 75.

(41) Brenner, T. M.; Egger, D. A.; Kronik, L.; Hodes, G.; Cahen, D. *Nature Reviews Materials* **2016**, *1*, 15007.

(42) Xing, G.; Mathews, N.; Sun, S.; Lim, S. S.; Lam, Y. M.; Grätzel, M.; Mhaisalkar, S.; Sum, T. C. *Science* **2013**, *342* (6156), 344−347.

(43) Chang, S. H.; Lin, K.-F.; Cheng, H.-M.; Chen, C.-C.; Wu, W.-T.; Chen, W.-N.; Wu, P.-J.; Chen, S.-H.; Wu, C.-G. *Sol. Energy Mater. Sol. Cells* **2016**, *145*, 375−381.

(44) Ledinsky, M.; Löper, P.; Niesen, B.; Holovsky, J.; Moon, S.-J.; Yum, J.-H.; De Wolf, S.; Fejfar, A.; Ballif, C. *J. Phys. Chem. Lett.* **2015**, *6* (3), 401−406.

(45) Brivio, F.; Frost, J. M.; Skelton, J. M.; Jackson, A. J.; Weber, O. J.; Weller, M. T.; Goni, A. R.; Leguy, A. M. A.; Barnes, P. R. F.; Walsh, A. *Phys. Rev. B: Condens. Matter Mater. Phys.* **2015**, *92* (14), 92.

(46) Bag, M.; Renna, L. A.; Adhikari, R. Y.; Karak, S.; Liu, F.; Lahti, P. M.; Russell, T. P.; Tuominen, M. T.; Venkataraman, D. *J. Am. Chem. Soc.* **2015**, *137* (40), 13130−13137.

(47) Quarti, C.; Grancini, G.; Mosconi, E.; Bruno, P.; Ball, J. M.; Lee, M. M.; Snaith, H. J.; Petrozza, A.; Angelis, F. D. *J. Phys. Chem. Lett.* **2014**, *5* (2), 279−284.

(48) Chen, T.; Foley, B. J.; Ipek, B.; Tyagi, M.; Copley, J. R.; Brown, C. M.; Choi, J. J.; Lee, S.-H. *Phys. Chem. Chem. Phys.* **2015**, *17* (46), 31278−31286.

(49) Zhu, H.; Miyata, K.; Fu, Y.; Wang, J.; Joshi, P. P.; Niesner, D.; Williams, K. W.; Jin, S.; Zhu, X. Y. *Science* **2016**, *353* (6306), 1409.

(50) Dou, L.; Yang, Y. M.; You, J.; Hong, Z.; Chang, W. H.; Li, G.; Yang, Y. *Nat. Commun.* **2014**, *5*, 5404.

(51) Deng, W.; Zhang, X.; Huang, L.; Xu, X.; Wang, L.; Wang, J.; Shang, Q.; Lee, S. T.; Jie, J. *Adv. Mater.* **2016**, *28*, 2201.

(52) Hu, X.; Zhang, X.; Liang, L.; Bao, J.; Li, S.; Yang, W.; Xie, Y. *Adv. Funct. Mater.* **2014**, *24* (46), 7373−7380.

(53) Wang, F.; Mei, J.; Wang, Y.; Zhang, L.; Zhao, H.; Zhao, D. *ACS Appl. Mater. Interfaces* **2016**, *8* (4), 2840−6.

(54) Deng, H.; Dong, D.; Qiao, K.; Bu, L.; Li, B.; Yang, D.; Wang, H.-E.; Cheng, Y.; Zhao, Z.; Tang, J.; et al. *Nanoscale* **2015**, *7* (9), 4163−4170.

(55) Horváth, E.; Spina, M.; Szekrényes, Z.; Kamarás, K.; Gaal, R.; Gachet, D.; Forró, L. *Nano Lett.* **2014**, *14* (12), 6761−6766.

(56) Deng, H.; Yang, X.; Dong, D.; Li, B.; Yang, D.; Yuan, S.; Qiao, K.; Cheng, Y. B.; Tang, J.; Song, H. *Nano Lett.* **2015**, *15* (12), 7963−9.

(57) Gao, L.; Zeng, K.; Guo, J.; Ge, C.; Du, J.; Zhao, Y.; Chen, C.; Deng, H.; He, Y.; Song, H.; Niu, G.; Tang, J. *Nano Lett.* **2016**, *16* (12), 7446−7454.

(58) Casaluci, S.; Cina, L.; Matteocci, F.; Lugli, P.; Di Carlo, A. *IEEE Trans. Nanotechnol.* **2016**, *15* (2), 255−260.

(59) Ding, J.; Du, S.; Zuo, Z.; Zhao, Y.; Cui, H.; Zhan, X. *J. Phys. Chem. C* **2017**, *121* (9), 4917−4923.

(60) Qian, L.; Sun, Y.; Wu, M.; Xie, D.; Ding, L.; Shi, G. *Adv. Mater.* **2017**, *29*, 1606175.

(61) Kang, D. H.; Pae, S. R.; Shim, J.; Yoo, G.; Jeon, J.; Leem, J. W.; Yu, J. S.; Lee, S.; Shin, B.; Park, J. H. *Adv. Mater.* **2016**, *28* (35), 7799−806.